Synthesis and thermal stability of *cis*-dichloro[*(E)*-ethyl-2-(2-((8-hydroxyquinolin-2-il)methylene)hidrazinyl)acetate-κ^2*N*]-palladium(II) complex

Nebojša N. Begović[1] · Milica M. Vasić[2] · Vladimir A. Blagojević[3] · Nenad R. Filipović[4] · Aleksandar D. Marinković[5] · Aleksandar Malešević[6] · Dragica M. Minić[2]

✉ Dragica M. Minić
dminic@ffh.bg.ac.rs

[1] Institute of General and Physical Chemistry, Belgrade, Republic of Serbia

[2] Faculty of Physical Chemistry, University of Belgrade, Belgrade, Republic of Serbia

[3] Institute of Technical Sciences of the Serbian Academy of Science and Arts, Belgrade, Republic of Serbia

[4] Faculty of Agriculture, University of Belgrade, Belgrade, Republic of Serbia

[5] Faculty of Technology and Metallurgy, University of Belgrade, Belgrade, Republic of Serbia

[6] Faculty of Chemistry, University of Belgrade, Belgrade, Republic of Serbia

Abstract The structure of new *cis*-dichloro[*(E)*-ethyl-2-(2-((8-hydroxyquinolin-2-il)methylene)hidrazinyl)acetate-κ^2*N*]-palladium(II) complex was determined using a combination of XRD and IR measurements and DFT calculations. Inherent flexibility of its structure is evident from the com-plexity of its IR spectrum, which could only be theoretically reproduced as a combination of several closely related structures, involving rotation around C–O bond and changes in hydrogen interactions of its –OH group. Its thermal sta-bility and decomposition were studied non-isothermally, and the thermal decomposition mechanism was proposed using correlation with DFT calculations at the molecular level. It was determined that the initial degradation step consists of the release of Cl free radical, which then reacts with both the initial compound and the degradation products. Besides the endothermic steps, there are exothermic ones, contributing to the complex shape of the DSC curve, consisted of overlap-ping endothermic and exothermic peaks. Deconvolution of DTG curve allowed identification of primary fragments of the initial degradation process and, in conjunction with DFT calculations, construction of the most likely reaction mechanism.

Keywords Thermal decomposition · Reaction mechanism · DFT calculation · Reaction kinetics · Organometallic complex · Thermodynamics

Introduction

Organometallic complexes have been attracting much sci-entific attention due to their favorable chemical, physical and biological properties [1–3]. These make them poten-tially useful for various applications, where these com-pounds act as catalysts, biologically active molecules, precursors for synthesis of different materials, flame retardants, data storage materials [1–6], etc. Functional properties of complexes are always connected to their particular structure, while the changes in environmental conditions provoke structural transformations, which lead to changes in the favorable properties, limiting their prac-tical applications. Therefore, stability of organometallic complexes is very important characteristic for their potential applications. Although thermal stability, mecha-nism and kinetics of thermal decomposition of organometallic complexes have been widely studied in recent time [7–11], in most cases these studies have been performed using only experimental techniques, such as TG, DSC, XRD, FTIR, while attempts to confirm and explain these results by correlating them with the results of theo-retical computational methods have been very rare [12–15].

Palladium(II) complexes have been recognized as effective catalysts and pre-catalysts for a number of reac-tions [16–20], and potential metal-based anticancer drugs [21–23]. It has been considered that stabilization of palla-dium(II) complexes, by prevention of possible cis–trans isomerisation, can be achieved using chelate ligands [24]. Hydrazone complexes have been a focus of intense research for a number of years owing to the large variety of potential applications [25, 26]. Thermal stability of palla-dium(II) complexes has been considered an important issue [27–29]. The study of the effect of the basicity of the ligands on the enthalpies and the activation energies of thermal decomposition of palladium(II) chloride com-plexes with pyridine [30] has shown that complexes of type PdL2Cl2 lost two ligands in a single step, resulting in PdCl2, with no relationship between the enthalpy values of decomposition and the other properties of the complexes. In general, trans influence of one ligand in the square-planar complexes causes the first ligand to be released easier than the second. This results in an increase in the calculated values of activation energy and a decrease in the temperature of the onset of thermal degradation with increase in basicity of the ligands. It was reported that thermal decomposition of trans-bis(2-amino pyridine) dichloro palladium(II) complex, where palladium(II) is coordinated to two monodentate ligands [31], occurs through three steps, where two amino-pyridines are released. The mass loss in TG experiment occurred in two separate temperature regions: 533–598 K and 598–718 K, due to the trans influence strengthening the bond of the second ligand to the metal center.

This study represents a part of a multidisciplinary investigation of a series of palladium(II) complexes with NN bidentate chelate hydrazone ligands derived from ethyl hydrazino acetate (haOEt) and various N-heteroaromatic carbonyl compounds. The *cis*-dichloro[*(E)*-ethyl-2-(2-((8-hydroxyquinolin-2-il)methylene)hidrazinyl)acetate-κ^2N]-palladium(II) complex is examined in terms of thermal stability and mechanism of thermally induced decomposition. To this end, combination of experimental techniques (TG, DSC, XRD, FTIR) and theoretical calculations (DFT) is employed. In addition, this research can serve as a model for examinations of thermal decomposition mechanism of other organometallic complex compounds.

Experimental

Synthesis of *cis*-dichloro[*(E)*-ethyl-2-(2-((8-hydrox-yquinolin-2-il)methylene)hidrazinyl)acetate-κ^2N]-palladium(II) complex was performed using ethyl-hydrazinoacetate hydrochloride (Aldrich, 97%), 8-hydroxy-2-quinolin-aldehyde (Maybridge, 98%) and K2[PdCl4] (Aldrich, min 32.0% Pd). All of the employed reagents and solvents were of analytical grade and used without further purification. Synthesis was performed by adding a solution of ethyl-hydrazinoacetate hydrochloride (0.043 mol L-1) and 8-hydroxy-2-quinoline-aldehyde (0.043 mol L-1) in acetonitrile (10 mL) to a solution of K2[PdCl4] (0.143 mol L-1) in water (3.0 mL). The reac-tion mixture was heated and stirred at 328 K for 30 min. Yellow microcrystalline product was filtered off and rinsed consecutively with water, acetonitrile and diethyl ether. The product was recrystallized from ethanol. Elemental analysis (C, H, N, S) was performed by the standard micromethods using the ELEMENTAR Vario EL III CHNSO analyzer. Thermogravimetric analyses were con-ducted using a Q500 TGA (TA Instruments) with sample weights of 10.0 ± 0.5 mg, in nitrogen atmosphere with gas flow rate of 50 mL min-1, at heating rates of 5, 10 and 20 K min-1 in platinum crucible. DSC measurements were carried out using DSC Q1000 (TA Instruments) with typ-ical sample weight of 2.0 ± 0.2 mg, in aluminum crucible, in nitrogen atmosphere with gas flow rate of 50 mL min-1 at constant heating rates of 2–40 K min-1. Peak decon-volution process for both DSC and DTG curves included a gradual process of deconvoluting the curve to the minimum possible number of peaks, starting from 2 and working up, using isoconversional curves as a test.

The X-ray powder diffraction (XRD) spectra were obtained on Philips PW-1710 automated diffractometer, using Cu Ka line, operated at 40 kV and 30 mA, in Bragg–Brentano geometry. The instrument was equipped with diffracted beam curved graphite monochromator and Xe-filled proportional counter. Indexing of powder XRD peaks and space group determination was performed using N-TREOR09 [32] as implemented within Expo2014 [33] program packet. For the ab initio crystal structure solution from diffraction data, the FOX [34] program was used. Rietveld analysis of X-ray powder diffraction data was done using MAUD [35] program, while the calculation of XRD pattern from cif file was performed using RIETAN-FP [36] software. Infrared (IR) spectra were recorded on a Thermo Scientific Nicolet 6700 FTIR spectrophotometer by the attenuated total reflection (ATR) technique in the region 4000–400 cm-1. DFT calculations on molecular systems were performed using Gaussian 09 [37] and ORCA version 3.0.3 [38] program package. Gaussian package was used for structure optimization and frequency analysis. All structures were fully optimized using C-PCM solvation method with Klamt [39] radii. Hybrid HF/DFT method was used for the calculations, with a combination of the three-parameter Becke [40] exchange functional and the Lee–Yang–Parr (B3LYP) [41] non-local correlation functional, and Becke's exchange functional combined with Perdew's [42] (BP86) non-local correlation functional. Orca package was employed for constraint relaxed surface scan at same theoretical level as in Gaus-sian 09, using COSMO solvation model. In addition, for calculations with Orca package, exchange and correlation functionals of Perdew, Burke and Ernzerhof (PBE) [43] were also used. The topology analysis of wave function proposed by Bader [44] was used for analyzing electron density ("atoms in molecules" theory (AIM) [44], also known as "the quantum theory of atoms in molecules" (QTAIM)), by program Multiwfn [45]. The same program was used for calculations of Fukui [46] and dual descriptor [47] functions which allowed us to predict the most reac-tive sites in molecule. The natural bond orbital analysis (NBO) [48] was performed with NBO program version 5.G. The localized molecular orbital energy decomposition analysis (LMOEDA) [49] of covalent bonds was performed

with the quantum chemistry program package GAMESS [50, 51] in which the LMOEDA method was implemented by the authors. The LMOEDA program uses existing programs in GAMESS to perform DFT calculations at the same basis sets and theoretical levels as used with Gaussian 09 programs package during molecule optimization stage. Elucidation of vibrational spectra of calculated structures was conducted using potential energy distribution (PED) analysis implemented in VEDA package [52].

Results and discussion

Structural characterization of the complex

After recrystallization of product from ethanol, the reaction yield was 89%. Elemental analysis has shown that the stoichiometric formula of the product is $C_{14}H_{15}Cl_2N_3O_3Pd$ (MW = 450.61). Experimentally determined composition was 37.43% C (calculated 37.32%), 3.39% H (calculated 3.36%), 9.51% N (calculated 9.33%). Structural characterization of complex was performed using powder XRD, Fig. 1, in combination with IR, Fig. 4. Complex crystallizes into triclinic lattice within $P\bar{1}$ space group, with preferential orientation along b-axis and asymmetrical needle-shaped crystallites. Detailed results of Rietveld analysis are shown in Table 1.

Figure 2a, b shows detailed structure of the complex obtained from XRD analysis and optimized in a quantum chemical calculation. Palladium center is coordinated with a quinoline nitrogen (N7), hydrazone nitrogen (N14) and two chlorine atoms (Cl_{12} and Cl20) in a slightly distorted square-planar geometry. Because of the presence of OH group in the vicinity of the metal center, the chlorine atom Cl20 is in an out-of-the-plane configuration, with dihedral angle (Cl20–Pd11–N7–N14) of 165°. Generally speaking, the molecule can be divided into two parts, aromatic and aliphatic. The aromatic part is relatively rigid, with p-stacking between the aromatic parts of neighboring mole-cules, while the aliphatic part is quite flexible. This struc-ture allows for the formation of intra- and intermolecular hydrogen bonds (Fig. 2b) between hydrogen and chlorine atoms. Intramolecular hydrogen bond can be formed between O19-H38 and Cl20 and between N15-H27 and Cl12. Intermolecular hydrogen bonds can be formed between hydrazone H27a from one molecule and Cl20b from the neighboring molecule, as shown in Fig. 2b. This shows that the distances between H27a and the two chlo-rines Cl12a (same molecule) and Cl20b (neighboring molecule) are 2.78 and 2.63 A˚ , respectively. Due to this difference in distances, the interaction of H27a with chlo-rine Cl20b is stronger than with chlorine Cl12a creating favorable conditions for intermolecular reaction between two neighboring molecules.

More insight into the interactions in palladium coordi-nation sphere was gained using natural bond order (NBO) analysis (Fig. 3) and localized molecular orbital energy decomposition analysis (LMOEDA). Optimized structure of the complex shows that the length of Pd11–Cl20 and Pd11–Cl12 bonds is 2.372 and 2.352 A˚ , respectively, both longer than Pd–Cl bond in PdCl2 (2.31 A˚). This is a con-sequence of nN ! r interaction, which leads to increased population in the anti-bonding orbital, reducing its bond order. Observed hydrogen bonds between the chlorine atoms and the adjacent hydrogen atoms reduce the natural charge on chlorine atoms to -0.244 on Cl12 and -0.240 on Cl20. NBO analysis also shows that the strength of donor–acceptor interaction is 12.24 kJ/mol for nCl20 !r and 4.61 kJ mol-1 for nCl12 ! r Based on their bond lengths, the character of Pd–Cl bonds can be described as predominantly ionic [48]. This reduction in the natural charge on Cl atoms also leads to the weakening of the Pd–Cl bond.

LMOEDA calculations also give information on the interactions of PdCl2 group and the rest of the complex (Table 2), through Pd–N interactions. It was calculated that the overall interaction of PdCl2 and the rest of the molecule is -315.6 kJ mol-1, which equals to an average of -157.8 kJ mol-1 per each Pd–N bond. Relative contribu-tions of different effects on this interaction indicate the presence of both ionic and covalent character of the bond, typical of donor–acceptor/coordinative bonding to the metal center [48].

In order to compare Pd–Cl and Pd–N bonds, Bader analysis was performed (Table 1S Supplement). The val-ues of electron density and Laplacian indicate that Pd–N bonds are considerably stronger than Pd-Cl. In addition, two Pd-Cl bonds exhibit markedly different values of ellipticity, which can be correlated with much stronger donor–acceptor interactions of Cl20 with adjacent H38 than that of Cl12 with its adjacent H27. This indicates that Cl20 would be the first one released from the complex molecule.

Vibrational analysis yielded more details on O–H and N–H interactions (Fig. 4). Individual vibrations in IR spectra were assigned through correlation with DFT cal-culations and potential energy distribution (PED) using.

VEDA software package and GaussView software for visual verification of vibrational modes (Table 2S). There are two regions of characteristic vibrations, 3400–3700 and 1000–1800 cm-1. Vibrations in 3400-3700 cm-1 region can be assigned to O–H and N–H stretching vibrations, while vibrations in 1000–1800 cm-1 region can be assigned to C=O, C–C and N–C vibrations. The calculated spectra have shown that a single structure could not entirely reproduce the experimental form of IR spectrum, due to flexibility of OH group in the molecule. It was found that the features in the spectrum can only be reproduced through several different structures resulting from rotation around C3–C4–O19–H38 dihedral angle in the range 0–66 (Fig. 5). Relaxed scan on the dihedral angle C3–C4–O19–H38 (Fig. 1S) shows that the energy barrier for rotation around C4–O19 bond is around 5 kJ mol-1. This suggests that the flexibility of the structure would allow hydrogen H38 to assume any orientation within this range of angles, resulting in the broad peak of OH stretching vibration in IR spectrum. The minima of energy profile for rotation around dihedral angle C3–C6–O1–H15 are at 66.1 and 170, with most stable structure corre-sponding to the angle of 66.1, which corresponds to the structure where H38 forms hydrogen bond with Cl20, as found by NBO and Bader analysis, Table 1S. This indi-cates that the hydroxyl group proton H38 could form hydrogen bonds not only to Cl20, but also to N7 and most likely also coordinates toward Pd center. Taking into consideration a combination of these structures, containing relatively minor structural differences, a good agreement with experimental IR spectrum was achieved.

Thermal stability

The fully reproducible TG and DSC curves were used for detailed thermal analysis of the complex. Non-isothermal measurements of the complex show that it is thermally stable up to 460 K, after which it undergoes complex thermal decomposition (Fig. 6). In the non-isothermal DSC curves, this manifests as a complex asymmetric exothermic peak preceded by another structural transformation around 330 K, which originates from structural reorganization of the ligand in the crystal structure, and it was also observed in other Pd complexes with similar ligands [31]. DFT calculations of the rotation around C16–C17 bond show that the energy barrier for this process is only around 14 kJ mol-1, while calculated energy barriers for rotation around the other bonds are significantly higher. This indi-cates that the rotation around C16–C17 bond together with the rotation around C4–O19 bond is the most likely cause of the observed structural transformation. The pattern of DSC curve changes from two clearly visible overlapping peaks at lower heating rates (2–10) to a single asymmetric complex peak at higher heating rates (20 and above). Full DSC data are available in the Supplement. This indicates different thermal activations of the individ-ual steps of the process of thermal degradation. The overall values of the apparent activation energies were determined using the position of the global maxima of the experimental peaks (Fig. 6). The overall values of the apparent activa-tion energy corresponding to lower heating rates are (810 ± 50) kJ mol-1 and only (270 ± 10) kJ mol-1 for higher heating rates. In addition, the shape of the curve of the effective values of the apparent activation energies at different reaction conversion degrees (Fig. 7), calculated using the integral isoconversional KAS method [53, 54], indicates that the process of thermal degradation is not a single-step process, but occurs with a change in the limit-ing step during the thermal degradation. The effective values of the apparent activation energies at different reaction conversion degrees are presented without errors, considering that these curves are used only to illustrate the complexity of the degradation process.

DSC curves contain overlapping endothermic and exothermic processes which could not be separated to a satisfactory degree at low heating rates. At higher heating tion energy corresponding to lower heating rates are (810 ± 50) kJ mol-1 and only (270 ± 10) kJ mol-1 for higher heating rates. In addition, the shape of the curve of the effective values of the apparent activation energies at different reaction conversion degrees (Fig. 7), calculated using the integral isoconversional KAS method [53, 54], indicates that the process of thermal degradation is not a single-step process, but occurs with a change in the limit-ing step during the thermal degradation. The effective values of the apparent activation energies at different reaction conversion degrees are presented without errors, considering that these curves are used only to illustrate the complexity of the degradation process.

DSC curves contain overlapping endothermic and exothermic processes which could not be separated to a satisfactory degree at low heating rates. At higher heating rates, DSC data were deconvoluted into three peaks, where the values of

activation energies of peaks 2 and 3 in DSC curve indicate that these correspond to peaks 1 and 2 in DTG curves (Supplement). Taking into account that DTG curves could be deconvoluted for both low and high heating rates, these data were used for further discussion of the mechanism of individual decomposition steps. The onset of the thermal decomposition in TG is around 460 K and occurs with a rapid mass loss. The mass loss slows down a bit after 490, and at 515 K, the sample loses around 19 mass%. Considering that TG curve recorded up to 620 K shows continual mass loss above 500 K, our anal-ysis of thermal degradation data was restricted to the region up to 515 K. In order to propose which fragments are released during each step of the complex decomposition process, DTG curves were deconvoluted using Fraser–Suzuki function (Fig. 8). The data at different heating rates were deconvoluted to a different number of peaks, due to the fact that isoconversional Ea curves from DTG data indicate that peaks 1 and 2 represent the same individual processes at different heating rates. Since the high heating rate data could not be deconvoluted with addition of only one peak (Peak 3), Peak 4 was added to account for difference between the low heating rate and high heating rate curves. These data were correlated with DFT calcu-lations and previously published results of TG-MS mea-surements of related compounds [24] to identify most likely products. This shows that the loss of mass during decomposition can be separated into three distinct contri-butions at lowers heating rates and four at higher heating rates, as a consequence of the change in mechanism and the limiting step. A broad deconvoluted peak, observed at both low and high heating rates, corresponds to a fragment of relatively large mass, which diffuses slower than the other lighter fragments. The release of this fragment from the system was incomplete at the end of TG measurement, as can be seen in Fig. 8. This would lead to discrepancy in observed and calculated mass loss. The remaining two deconvoluted peaks at lower heating rates were assigned to the release of HCl and water molecules, while the remaining three deconvoluted peaks at higher heating rates were assigned to the release of HCl, C2H5 and water, respectively. This suggests that higher heating rates lead to faster fragmentation of the aliphatic part of the complex. Molecular masses and assigned fragments corresponding to individual deconvoluted DTG peaks at three different heating rates are given in Table 3.

Besides the release of different degradation products, the mechanism of thermal degradation involves several steps of intra- and intermolecular reactions. In order to discuss potential reaction sites in the initial complex, topological analysis of the Fukui functions f-(r) and f?(r) [46] and dual descriptor for chemical reactivity [47] were calculated (Fig. 9). These analyses (Fig. 9) show that chlorine atoms are the preferred sites for an electrophilic attack, excluding the aromatic system which is generally stable, while car-boxylic oxygen and amino group represent preferred sites for a nucleophilic attack. Dual descriptor analysis also shows that, excluding the aromatic system, chlorine atoms for electrophilic, and hydrazone nitrogen and carboxylic group for nucleophilic attack, represent the most reactive sites.

Considering all the evidence indicating that chlorine represents the likely reaction site, as well as the appearance of HCl during the early stage of thermal decomposition of complex, we considered dissociation of Pd-Cl bonds as the initial step of thermal degradation. These bonds are rela-tively long and weak, and potential energy curves of bond dissociation (Supplement) show that Pd–Cl20 (energy barrier of 35 kJ mol-1) dissociates much easier than Pd–Cl12 (120 kJ mol-1). This would result in the formation of Cl radical and the transformed form of 1, KOMP-1. This Cl radical can react further through two different reaction mechanisms (RA- and RB-path): with the initial complex (intermolecular reaction, Step RA-1), as well as with KOMP-1 (intramolecular reaction Step RB-2). Based on the unit cell structure (Fig. 2a), only one half of molecules of the complex possess the necessary conformation for the intermolecular reaction (RA-path) to form HCl (the enthalpy of this reaction is -1.72 kJ mol-1). The other half of molecules can react intramolecularly (RB-path), forming the Cl radical with enthalpy of reac-tion 7.39 kJ mol-1. Subsequently, formed HCl leaves the system or, through a condensation reaction (steps RB-4 and RA-3), forms a water molecule, which is then released from the system, as found in TG. Potential energy curve, Fig. 3S, shows that this reaction step would occur rela-tively easily in both reaction pathways. Due to a shorter reaction path of the chlorine radical in the intramolecular pathway, it should occur with a lower activation energy. After the loss of Cl20, the energy barrier for dissociation of Pd11–Cl12 bond (Fig. 4S) becomes even higher (around 150 kJ mol-1). Using the correlation of the experimental results with thermodynamic and kinetic aspects of these reaction steps from DFT calculations, two sets of potential equations (RA1-RA4 and RB1-RB5) describing reaction paths of thermal degradation of complex, at different heating rates, were proposed.

Analysis of DTG results (Table 3) indicates that, in addition to HCl and H2O, a heavier fragment appeared, with a mass around 90 at lower heating rates, and around 80 at higher heating rates. This is in good accordance with DFT calculations which have shown that Cl radical could provoke further fragmentation of formed intermediary complexes through breaking of C11–N3 bond (fragment mass around 90) and the creation of an aliphatic fragment ClCH2COOC2H5. This occurs with an energy barrier of 160–200 kJ mol-1, which is higher than that for the for-mation of molecules HCl and H2O. In both cases, this fragmentation starts at the same site, resulting in the same aliphatic fragment, which decomposes further, at higher

heating rates, into lighter fragments observed in DTG measurements, Fig. 8. Taking into consideration all of this, the mechanism of further degradation can be presented as:

$$\text{KOMP-2A} + {}^{\cdot}\text{Cl} \rightarrow \text{Ar-1} + \text{ClCH}_2\text{COOC}_2\text{H}_5 \quad \text{RC-1}$$

$$\text{HOH}^{\cdots}\text{KOMP-3A} + {}^{\cdot}\text{Cl} \rightarrow \text{HOH}^{\cdots}\text{Ar-2} + \text{ClCH}_2\text{COOC}_2\text{H}_5 \quad \text{RC-2}$$

$$\text{HOH}^{\cdots}\text{KOMP-2B} + {}^{\cdot}\text{Cl} \rightarrow \text{HOH}^{\cdots}\text{Ar-3} + \text{ClCH}_2\text{COOC}_2\text{H}_5 \quad \text{RC-3}$$

$$\text{KOMP-2B} + {}^{\cdot}\text{Cl} \rightarrow \text{Ar-3} + \text{ClCH}_2\text{COOC}_2\text{H}_5 \quad \text{RC-4}$$

According to deconvoluted curves, Fig. 8, it could be expected that the formation of the heavier fragment would occur during the initial step of thermal degradation of the complex, in parallel with the release of HCl and H_2O, however, with significantly lower reaction rates, due to higher energy barriers. After the release of HCl and H_2O, the energy barrier for fragmentation decreases further, which can be correlated with the gradual mass loss in the temperature region above 500 K. Formed aliphatic frag-ment $ClCH_2COOC_2H_5$ would, according to the Barton mechanism [55], react with H_2O to produce an alcohol fragment of the mass of 103 and HCl:

$$\text{ClCH}_2\text{COOC}_2\text{H}_5 + \text{HOH} \rightarrow \text{HOCH}_2\text{COOC}_2\text{H}_5 + \text{HCl} \quad \text{RC-4}$$

Conclusions

Thermal stability and mechanism of thermal degradation of the new *cis*-dichloro[*(E)*-ethyl-2-(2-((8-hydroxyquinolin-2-il)methylene)hidrazinyl)acetate-κ^2N]-palladium(II) com-plex were investigated using a combination of experi-mental and theoretical methods. Complex was thermally stable up to the temperature of 460 K, after which it undergoes a process of thermal degradation through mul-tiple overlapping endothermic and exothermic steps. The overall enthalpy of the observed portion of thermal degradation is in the range 20–25 kJ mol^{-1}, depending on the heating rate. DTG curves at different heating rates were deconvoluted to determine the approximate masses of fragments released in the initial stages of thermal degra-dation. The entire process of thermal degradation is verycomplex and occurs through either inter- or intramolecular pathway, and diffusion of released fragments, where the mechanism and the kinetics depend on the heating rate. The intermolecular mechanism exhibits significantly lower values of activation energies and enthalpies, leading to its higher probability at lower heating rates, as observed experimentally. The intramolecular mechanism exhibits higher values of activation energies and enthalpies, making it more prevalent at higher heating rates. The fragmentation of the aliphatic part of the ligand can occur only through the attack of Cl radical at C11, leading to gradual degra-dation of the ligand in DTG due to limited availability of Cl radical. At higher heating rates (20 K min-1), it is likely that the fragment created through this reaction decomposes further through reaction with H2O according to Barton mechanism, leading to the appearance of two smaller fragments at higher heating rates, compared to one larger fragment at lower heating rates.

References

1. Legzdins P, Rettig SJ, Sanchez L. Synthesis, characterization, and some chemical properties of unusual 16-electron dialkyl(η^5-cyclopentadienyl)nitrosylmolybdenum and -tungsten Complexes. Organometallics. 1988;7:2394–403.
2. McDonagh AM, Humphrey MG, Samoc M, Luther-Davies B. Organometallic complexes for nonlinear optics. 17. synthesis, third-order optical nonlinearities, and two-photon absorption cross section of an alkynylruthenium dendrimer. Organometallics. 1999;18:5195–7.
3. Filipović NR, Bjelogrlić S, Todorović TR, Blagojević VA, Muller CD, Marinković A, Vujćić M, Janović B, Malešević AS, Begović N, Senc´anski M, Minić DM. Ni(II) complex with bishydrazone ligand: synthesis, characterization, DNA binding studies and proapoptotic and pro-differentiation induction in human cancerous cell lines. RSC Adv. 2016;6:108726–40.
4. Meneghetti MR, Meneghetti SMP. Sn(IV)-based organometallics as catalysts for the production of fatty acid alkyl esters. Catal Sci Technol. 2015;5:765–71.
5. Abd El-Wahab H, Abd El-Fattah M, Ahmed AH, Elhenawy AA, Alian NA. Synthesis and characterization of some arylhydrazone ligand and its metal complexes and their potential application as flame retardant and antimicrobial additives in polyurethane for surface coating. J Organomet Chem. 2015;791:99–106.
6. Chen Z, Wu Y, He C, Wang B, Gu D, Gan F. Insights into the physical basis of metal(II) hydrazone complexes with isoxazole and barbituric acid moieties for recordable blu-ray media. Synth Met. 2010;160:2581–6.
7. Shankarwar SG, Nagolkar BB, Shelke VA, Chondhekar TK. Synthesis, spectral, thermal and antimicrobial studies of transition metal complexes of 14-membered tetraaza[N4] macrocyclic ligand. Spectrochim Acta A. 2015;145:188–93.
8. Selvakumar R, Geib SJ, Premkumar T, Govindarajan S. Syn-thesis, spectroscopic, thermal and XRD studies of aminoguanidinium copper and cadmium oxalates. J Therm Anal Calorim. 2016;124:375–85.
9. Harmatová Z, Jóna E, Medvecká J, Valigura D, Mojumdar SC. Thermal properties of solid complexes with biologically important heterocyclic ligands. J Therm Anal Calorim. 2015;119:915–9.

10. Selvakumar R, Geib SJ, Premkumar T, Govindarajan S. Syn-thesis, structure and thermal properties of a new 1D magnesium sulfoacetate coordination polymer. J Therm Anal Calorim. 2015;121:943–9.
11. Jin CW, Shen PP, Ren N, Geng LN, Zhang JJ. Structure, lumi-nescent and thermal properties of two novel lanthanide com-plexes with 3,4-diethoxybenzoic acid and 5,5′-dimethy-2,2′-bipyridine. J Therm Anal Calorim. 2016;126:1549–58.
12. Begović NN, Blagojević VA, Ostojić SB, Radulović AM, Poleti D, Minić DM. Thermally activated 3D to 2D structural trans-formation of $[Ni_2(en)_2(H_2O)_6(pyr)]\cdot 4H_2O$ flexible coordination polymer. Mater Chem Phys. 2015;149–150:105–12.
13. Ristović MŠ, Pavlović MG, Zlatar M, Blagojević V, Anđelković K, Poleti D, Minić DM. Kinetics, mechanism, and DFT calculations of thermal degradation of a Zn(II) complex with *N*-benzyloxycar-bonylglycinato ligands. Monatsh Chem. 2012;143:1133–9.
14. Hao Y, Peng J, Hu S, Li J, Zhai M. Thermal decomposition of allyl-imidazolium-based ionic liquid studied by TGA–MS anal-ysis and DFT calculations. Thermochim Acta. 2010;501:78–83.
15. Thomson LM, Hall MB. Theoretical study of the thermal decomposition of N, N′-Diacyl-N, N′-Dialkoxyhydrazines: a Comparison of HF, MP2, and DFT. J Phys Chem A. 2000;104: 6247–52.
16. Peris E, Loach JA, Mata J, Crabtree RH. A Pd complex of a tridentate pincer CNC bis-carbene ligand as a robust homogenous Heck catalyst. Chem Commun. 2001;2:201–2.
17. Mino T, Shiotsuki M, Yamamoto N, Suenaga T, Sakamoto M, Fujita T, Yamashita M. Palladium-catalyzed allylic alkylation using chiral hydrazones as ligands. J Org Chem. 2001;66:1795–7.
18. Mino T, Shirae Y, Sakamoto M, Fujita T. Phosphine-free hydrazone-Pd complex as the catalyst precursor for a Suzuki-Miyaura reaction under mild aerobic conditions. J Org Chem. 2005;70:2191–4.
19. Karimi B, Enders D. New N-heterocyclic carbene palladium complex/ionic liquid matrix immobilized on silica: application as recoverable catalyst for the Heck reaction. Org Lett. 2006;8: 1237–40.
20. Chou CC, Yang CC, Syu HB, Kuo TS. Monomeric Pd(II) com-plexes with *trans*-chelated pyrazole ligands as effective pre-cat-alysts for Heck cross-coupling reaction under mild aerobic conditions. J Organometal Chem. 2013;745–6:387–92.
21. Teyssot ML, Jarrouse AS, Manin M, Chevry A, Roche S, Norre F, Beaudoin C, Morel L, Boyer D, Mahiou R, Gautier A. Metal-NHC complexes: a survey of anti-cancer properties. Dalton Trans. 2009;35:6894–902.
22. Kismali G, Emen FM, Yesilkaynak T, Meral O, Demirkiran D, Sel T, Kulcu N. The cell death pathway induced by metal halide complexes of pyridine and derivative ligands in hepatocellular carcinoma cells – necrosis or apoptosis? Eur Rev Med Pharmacol Sci. 2012;16:1001–12.
23. Ray S, Mohan R, Singh JK, Samantaray MK, Shaikh MM, Panda D, Ghosh P. Anticancer and antimicrobial metallopharmaceutical agents based on palladium, gold, and silver *N*-heterocyclic car-bene complexes. J Am Chem Soc. 2007;129:15042–53.
24. Begović NN, Blagojević VA, Ostojić SB, Micić DM, Filipović N, Andjelković K, Minić DM. Thermally induced structural trans-formations of a series of palladium(II) complexes with *N*-heteroaromatic bidentate hydrazone ligands. Thermochim Acta. 2014;592:23–30.
25. Krishamoorthy P, Sathyadevi P, Cowley AH, Butorac RR, Dharmaraj N. Evaluation of DNA binding, DNA cleavage, pro-tein binding and in vitro cytotoxic activities of bivalent transition metal hydrazone complexes. Eur J Med Chem. 2011;46:3376–87.
26. Suvarapu LN, Seo YK, Baek SO, Ammireddy VR. Review on analytical and biological applications of hydrazones and their metal complexes. J Chem. 2012;9:1288–304.
27. Masoud MS, Ali AE, El-Kaway MYA. Thermal properties of mercury(II) and palladium(II) purine and pyrimidine complexes. J Therm Anal Calorim. 2014;116:183–94.
28. Uivarosi V, Badea M, Aldea V, Chirigiu L, Olar R. Thermal and spectral studies of palladium(II) and platinum(IV) complexes with dithiocarbamate derivatives. J Therm Anal Calorim. 2013; 111:1177–82.
29. Da Silva C, Da Silva DAM, Rocha FV, Barra CV, Frem RCG, Netto AVG, Mauro AE, De Almeida ET. Synthesis, characterization and thermal behavior of palladium(II) complexes containing 4-iodopy-razole. J Therm Anal Calorim. 2014;117:1327–34.
30. Farran R, House JE. Thermal decomposition of complexes of palladium(II) chloride with substituted pyridines. J Inorg Nucl Chem. 1972;34:2219–23.
31. Gomez-Vaamonde C, Alvarez-Valdes A, Navarro-Ranninger MC, Masaguer JR. Synthesis and characterization of Pd(II) complexes with 2-aminopyridine. Transition Met Chem. 1984; 9:52–4.
32. Altomare A, Campi G, Cuocci C, Eriksson L, Giacovazzo C, Moliterni A, Rizzi R, Werner PE. Advances in powder diffraction pattern indexing: N-TREOR09. J Appl Cryst. 2009;42:768–75.
33. Altomare A, Cuocci C, Giacovazzo C, Moliterni A, Rizzi R, Cor-riero N, Falcicchio A. EXPO2013: a kit of tools for phasing crystal structures from powder data. J Appl Cryst. 2013;46:1231–5.
34. Favre-Nicolin V, Černy R. FOX, 'free objects for crystallogra-phy': a modular approach to ab initio structure determination from powder diffraction. J Appl Cryst. 2002;35:734–43.
35. Ferrari M, Lutterotti L. Method for the simultaneous determina-tion of anisotropic residual stresses and texture by X-ray diffraction. J Appl Phys. 1994;76:7246–55.
36. Izumi F, Momma K. Three-dimensional visualization in powder diffraction. Solid State Phenom. 2007;130:15–20.
37. Frisch MJ, Trucks GW, Pople JA. Gaussian 09. Revision B2. Pittsburgh: Gaussian Inc; 2009.
38. Neese F. The ORCA program system. Wiley Interdiscip Rev Comput Mol Sci. 2012;2:73–8.
39. Sinnecker S, Rajendran A, Klamt A, Diedenhofen M, Neese F. Calculation of solvent shifts on electronic g-tensors with the conductor-like screening model (COSMO) and its self-consistent generalization to real solvents (Direct COSMO-RS). J Phys Chem 2006;110:2235–45.

40. Becke AD. Density-functional exchange-energy approximation with correct asymptotic behavior. Phys Rev A. 1988;38:3098–100.
41. Lee C, Yang W, Parr RG. Development of the Colle-Salvetti correlation-energy formula into a functional of the electron density. Phys Rev B. 1988;37:785–9.
42. Perdew JP. Density-functional approximation for the correlation energy of the inhomogeneous electron gas. Phys Rev B. 1986;33: 8822–4.
43. Perdew JP, Burke K, Ernzerhof M. Generalized gradient approximation made simple. Phys Rev Lett. 1996;77:3865–8.
44. Bader RFW. Atoms in molecules: a quantum theory (Interna-tional series of monographs on chemistry). Oxford: Clarendon press; 1994.
45. Lu T, Chen F. Multiwfn: a multifunctional wavefunction ana-lyzer. J Comput Chem. 2012;33:580–92.
46. Parr R, Yang W. Density functional approach to the frontier-electron theory of chemical reactivity. J Am Chem Soc. 1984;106: 4049–50.
47. Morell C, Grand A, Toro-Labbe A. New dual descriptor for chemical reactivity. J Phys Chem A. 2005;109:205–12.
48. Weinhold F, Landis CR. Valency and bonding. New York: Cambridge University Press; 2005.
49. Su P, Li H. Energy decomposition analysis of covalent bonds and intermolecular interactions. J Chem Phys. 2009;131:014102.
50. Schmidt MW, Baldridge KK, Boatz JA, Elbert ST, Gordon MS, Jensen JH, Koseki S, Matsunaga N, Nguyen KA, Su SJ, Windus TL, Dupuis M, Montgomery JA. General atomic and molecular electronic structure system. J Comput Chem. 1993;14:1347–63.
51. Gordon MS, Schmidt MW, Dykstra CE, Frenking G, Kim KS, Scuseria GE. Theory and applications of computational chem-istry. Amsterdam: Elsevier; 2005.
52. Jamroz MH. Vibrational energy distribution analysis VEDA 4. Warsaw; 2004–2010.
53. Kissinger HE. Reaction kinetics in differential thermal analysis. Anal Chem. 1957;29:1702–6.
54. Akahira T, Sunose T. Method of determining activation deteri-oration constant of electrical insulating materials. Res Rep Chiba Inst Technol (Sci Technol). 1971;16:22–31.
55. Barton DHR, Bashiardes G, Fourrey JL. An improved preparation of vinyl iodides. Tetrahedron Lett. 1983;24:1605–8.

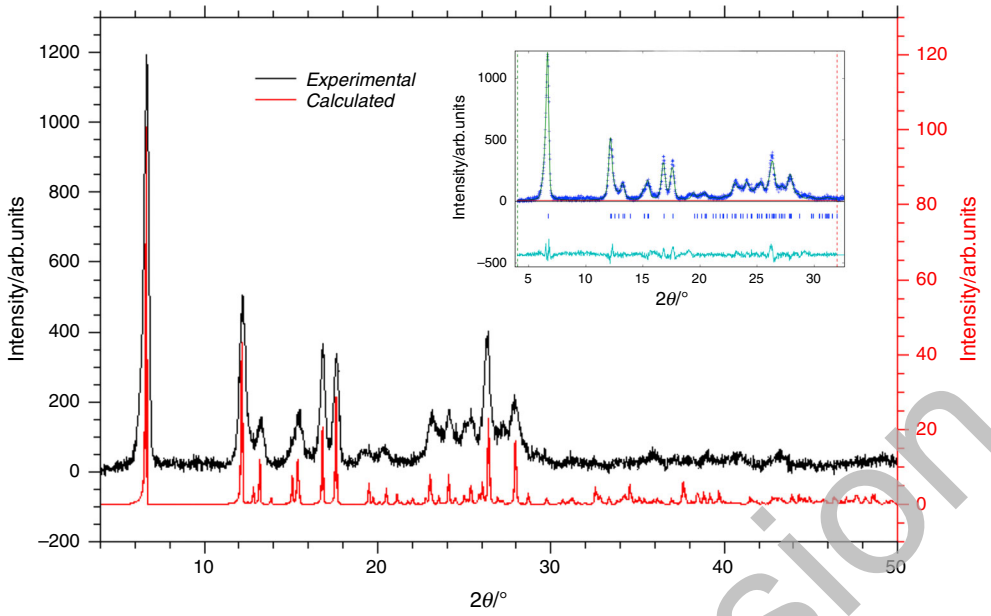

Fig. 1 Experimental XRD pattern of the complex and pattern calculated from *cif* file using RIETAN-FP software package, Rietveld analysis shown in *inset*

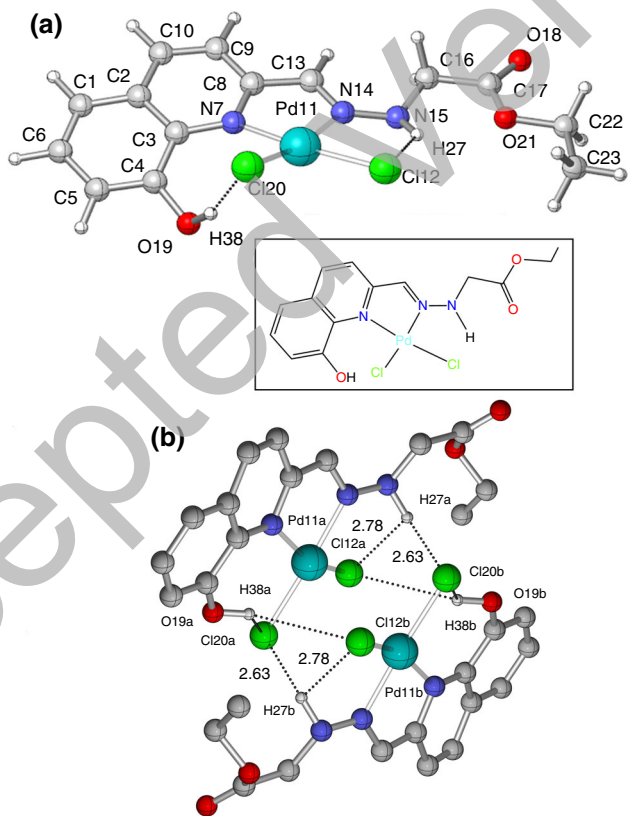

Fig. 2 **a** Optimized structure of the complex; **b** intermolecular bonding of two asymmetrical units of complex; hydrogen bonds are presented by *dotted lines*

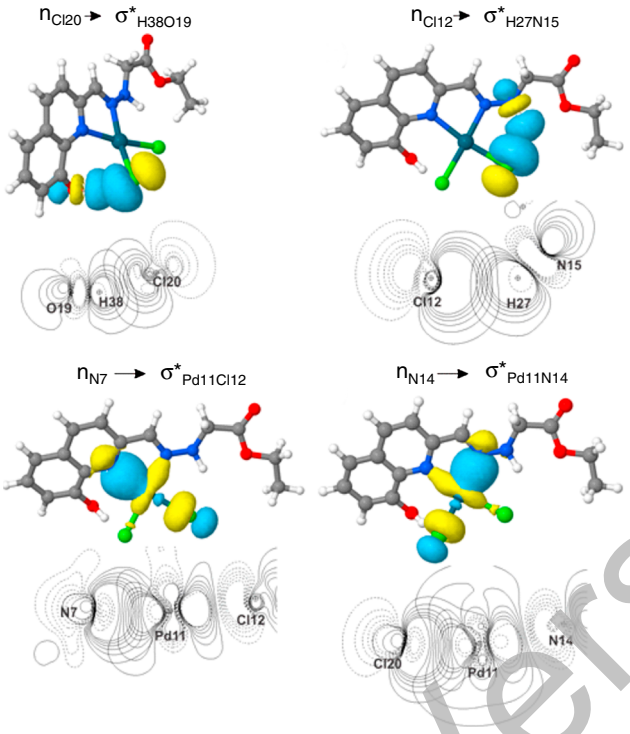

Fig. 3 Results of NBO analysis, where the orbital wave functions are positive in the *blue regions* and negative in the *yellow*. (Color figure online)

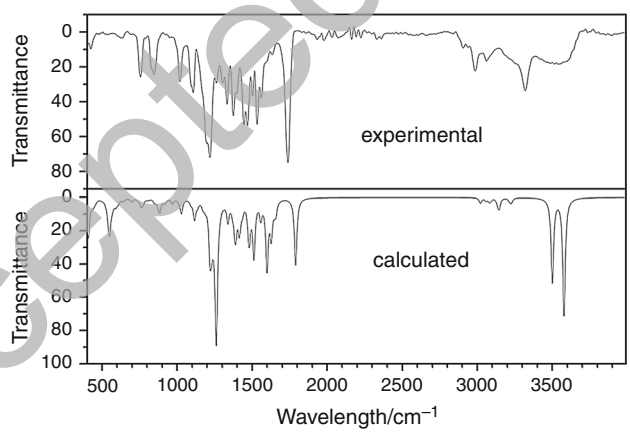

Fig. 4 Experimental (*top*) and calculated (*bottom*) IR spectra

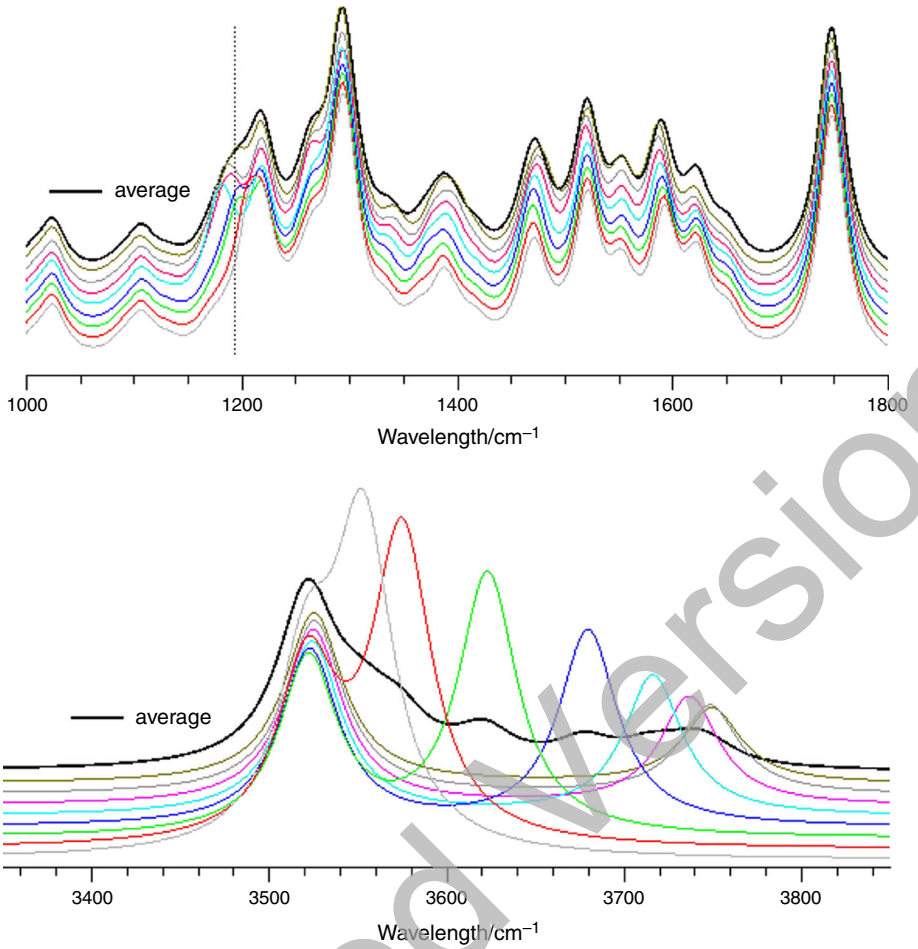

Fig. 5 Region of calculated IR spectra corresponding to C=O, C–C and C–N vibrations. *Vertical line* indicates the position of O–H bending vibration(*top*). Part of calculated IR spectra which represent N–H and O–H stretching vibration (*bottom*). Spectra in *black* represent the averaged spectra over all calculated values of dihedral angle

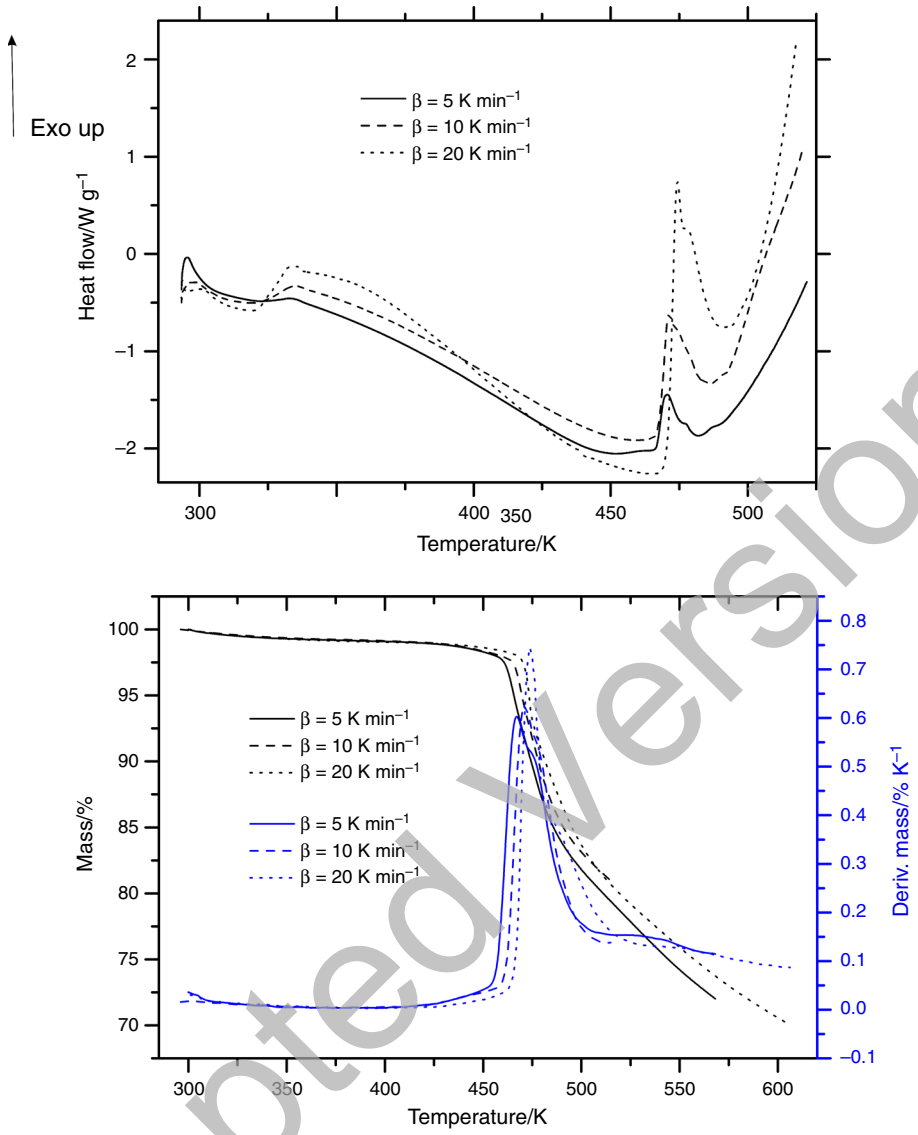

Fig. 6 Thermal analysis in temperature range 290–520 K

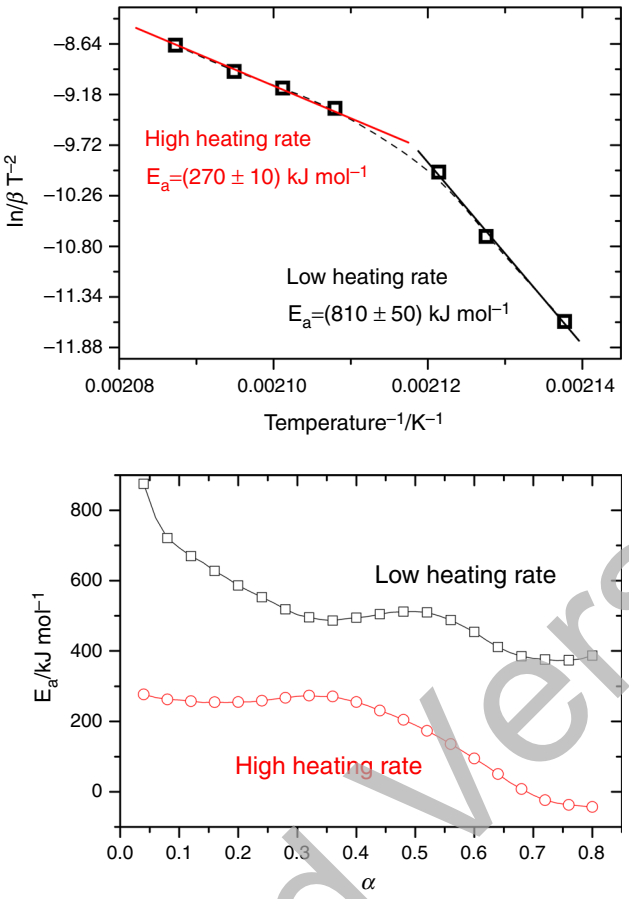

Fig. 7 Overall values of apparent activation energy determined using Kissinger [53] method (*top*); isoconversional Kissinger–Akahira–Sunose (KAS) [53, 54] method for experimental peaks (heating rates: low 2–10, high 20–40 K min^{-1}) (*bottom*)

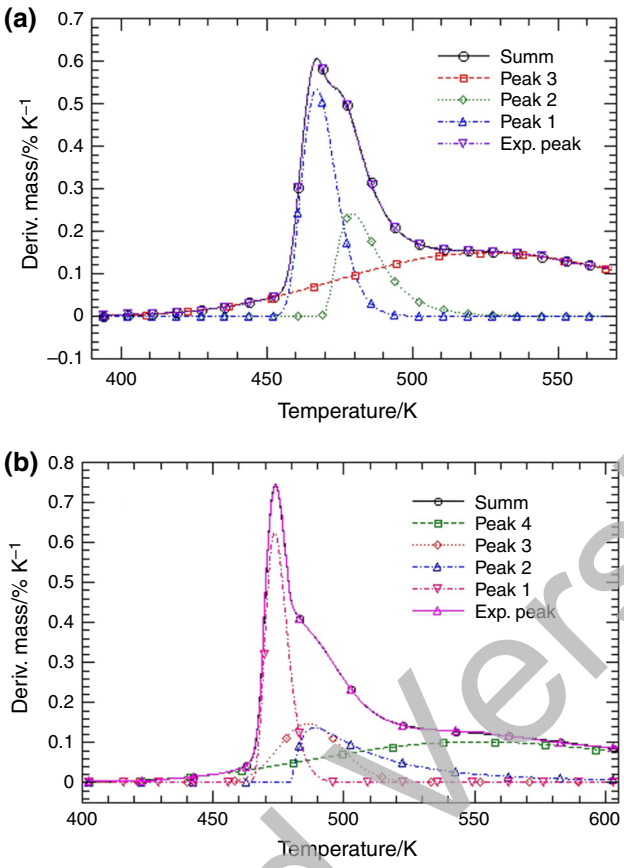

Fig. 8 DTG curves for thermal decomposition at 5 (**a**) and 20 (**b**) K min^{-1}. (Color figure online)

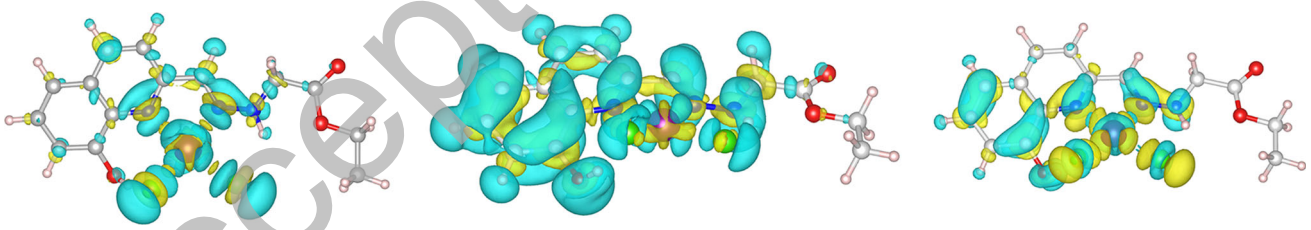

Fig. 9 Fukui functions $f^{-}(r)$ (*left*), $f^{+}(r)$ (*middle*) and dual descriptor function (*right*), for initial complex. *Blue color* represents the sufficient sites, while the *yellow color* represents the deficient sites

Table 1 Chemical formula and results of Rietveld analysis

Property	Complex in powder form
Molecular formula	(C14·H15·Cl2·N3·O3·Pd)
Formula weight	450.61
Crystal system	Triclinic
Space group	$P\bar{1}$
Z	2
Average crystal size/nm	>10,000
Microstrain/%	0.025 ± 0.001 (a-axis)
	0.095 ± 0.001 (c-axis)
a/Å	14.711 (2)
b/Å	8.479 (2)
c/Å	7.998 (2)
α/°	64.50 (1)
β/°	106.53 (1)
γ/°	112.24 (1)
V/Å^3	824.61
ρ/g cm^{-3}	1.815
Wavelength/Å	1.54056
*a**	0.831
*b**	−0.111
*c**	0.544
R0	1.56

Table 2 Results of LMOEDA calculation for PdCl2 group and the rest of the complex

Interaction	Energy per interaction/ kJ mol^{-1}
Electrostatic energy (es)	−145.48
Exchange energy (ex)	−99.48
Repulsion energy (rep)	306.18
Polarization energy (pol)	−114.57
DFT dispersion energy (dis)	−22.05
Total interaction energy hf or dft (e)	−75.40

Table 3 Molecular masses corresponding to individual fragments

Peak	Heating rate/K min^{-1}		
	5	10	20
First	36.96 (HCl)	35.03 (HCl)	31.10 (HCl)
Second	21.49 (H_2O)	21.91 (H_2O)	25.61 (C_2H_4)
Third	90.56 ($OCOC_2H_5$)	81.41 (ClC_2H_5)	20.45 (H_2O)
Fourth			79.96 (ClC_2H_5)

Intermolecular pathway at low heating rates

$Cl^{\cdot}$ + KOMP → HCl···KOMP-1A	RA-1,	$\Delta H_r^0 = -11.9$ kJ mol^{-1}
HCl···KOMP-1A → HCl + KOMP-1A	RA-2,	$\Delta H_r^0 = -4.6$ kJ mol^{-1}
HCl + KOMP-1A → HOH···KOMP-2A	RA-3,	$\Delta H_r^0 = +61.9$ kJ mol^{-1}
HOH···KOMP-2A → HOH + KOMP-2A	RA-4,	$\Delta H_r^0 = +3.8$ kJ mol^{-1}
		$\sum \Delta H_r^0 = +49.2$kJ mol^{-1}

Intramolecular pathway at high heating rates

KOMP → Cl···KOMP-1B	RB-1,	$\Delta H_r^0 = +7.4$ kJ mol^{-1}
Cl···KOMP-1B → HCl···KOMP-2B	RB-2,	$\Delta H_r^0 = +114.7$ kJ mol^{-1}
HCl···KOMP-2B → HCl + KOMP-2B	RB-3,	$\Delta H_r^0 = +15.1$ kJ mol^{-1}
HCl···KOMP-2B → HOH···KOMP-3B	RB-4,	$\Delta H_r^0 = +23.8$ kJ mol^{-1}
HOH···KOMP-3B → HOH + KOMP-3B	RB-5,	$\Delta H_r^0 = +17.5$ kJ mol^{-1}
		$\sum \Delta H_r^0 = +169.5$kJ mol^{-1}